Mechanistic patient-specific predictive correlation of tumor drug response with microenvironment and perfusion measurements

Jennifer Pascal[a,1], Elaine L. Bearer[a,b,1], Zhihui Wang[a,1], Eugene J. Koay[c], Steven A. Curley[d], and Vittorio Cristini[a,e,2]

Departments of [a]Pathology and [e]Chemical and Nuclear Engineering and Center for Biomedical Engineering, University of New Mexico, Albuquerque, NM 87131; Departments of [c]Radiation Oncology and [d]Surgical Oncology, The University of Texas MD Anderson Cancer Center, Houston, TX 77030; and [b]Division of Biology, California Institute of Technology, Pasadena, CA 91125

Edited* by Harry B. Gray, California Institute of Technology, Pasadena, CA, and approved July 16, 2013 (received for review January 10, 2013)

Physical properties of the microenvironment influence penetration of drugs into tumors. Here, we develop a mathematical model to predict the outcome of chemotherapy based on the physical laws of diffusion. The most important parameters in the model are the volume fraction occupied by tumor blood vessels and their average diameter. Drug delivery to cells, and kill thereof, are mediated by these microenvironmental properties and affected by the diffusion penetration distance after extravasation. To calculate parameter values we fit the model to histopathology measurements of the fraction of tumor killed after chemotherapy in human patients with colorectal cancer metastatic to liver (coefficient of determination $R^2 = 0.94$). To validate the model in a different tumor type, we input patient-specific model parameter values from glioblastoma; the model successfully predicts extent of tumor kill after chemotherapy ($R^2 = 0.7$–0.91). Toward prospective clinical translation, we calculate blood volume fraction parameter values from in vivo contrast-enhanced computed tomography imaging from a separate cohort of patients with colorectal cancer metastatic to liver, and demonstrate accurate model predictions of individual patient responses (average relative error = 15%). Here, patient-specific data from either in vivo imaging or histopathology drives output of the model's formulas. Values obtained from standard clinical diagnostic measurements for each individual are entered into the model, producing accurate predictions of tumor kill after chemotherapy. Clinical translation will enable the rational design of individualized treatment strategies such as amount, frequency, and delivery platform of drug and the need for ancillary non–drug-based treatment.

colorectal cancer liver metastasis | glioblastoma multiforme histopathology | contrast CT | patient drug response | mathematical modeling

Predicting the effects of chemotherapeutic drugs on tumor behavior in patients is vital to advancing knowledge in the fight against cancer. Computational methods of "mathematical pathology" developed through quantitative analysis of human tumor tissue have the potential to provide predictions of treatment outcomes in the clinical setting (1). Here, we develop our model using colorectal cancer (CRC) metastatic to liver from one cohort of patients as an example of intratumor perfusion properties. We then assess the general applicability of our model to predict response in other tumor types, that is, glioblastoma multiforme (GBM). We prospectively apply our model in vivo to a third cohort of subjects with metastatic CRC to liver using pretreatment contrast-enhanced computed tomography (CT) scans followed by correlation histopathology after treatment and surgical excision.

CRC metastatic to liver can be treated by surgical resection in the majority of cases. Metastases too large or numerous for primary excision are first treated with chemotherapy and then excised if possible, because chemotherapy alone is rarely curative (2, 3). This strategy works, but in only 30% of cases (4, 5). In other tumor types, such as GBM, outcomes are even worse. Thus, there is a pressing need for a deeper understanding of the mechanisms underlying the failure of chemotherapy. Conventional therapeutic drugs delivered intravenously, and therefore nonspecific in their distribution and targeting, result in comparable toxicity to normal cells, thus limiting dosage (6). To be effective, chemotherapeutic agents must travel through the blood vessels, extravasate into the interstitium, and diffuse through the tumor mass (7–9). Research testing drugs on cultured cells in monolayers fails to account for these physiological and biological aspects of drug delivery (10). Here we demonstrate that the most significant parameters for effective drug delivery are the fraction of blood volume within the tumor, the distribution of tumor vessel diameters, and the distance that drugs diffuse through tumor tissue. These parameter values differ among tumor types, and even in different individuals with similar tumor types, and thus cannot be predicted a priori but need to be measured on an individual basis.

Our model begins with a differential equation based on mathematical descriptions of diffusion and its parameters. From histopathological specimens we obtain a biophysical description of the vascular/tissue architecture upon which to formulate our mathematical model of drug perfusion within the tumor mass. We assume that the "kill zone" around viable tumor represents diffusion penetration distance. Using regression analysis, we retrospectively compare the model to the direct measurement of the size of the kill zone for each specimen and assess the biological relevance of the model formula and fitted parameter values. We then apply the model against primary tumors arising in tissue with vasculature different from that of the liver (i.e., patient samples of GBM biopsied after chemotherapy). GBM is the most malignant primary brain tumor and secretes high levels of vascular endothelial growth factor, inducing vascular proliferation. Despite its vascular density, GBM is highly resistant to chemotherapy and antiangiogenic therapies (11). Comparison of postchemotherapy biopsies of GBM with our model addresses questions of how tissue architecture and vascular distribution influence chemotherapeutic delivery in addition to validating the generality of our modeling approach. To demonstrate the power of our model for prospective clinical application, we test model predictions of cell kill based on parameters measured from pretreatment contrast-enhanced CT scans. The novelty of our approach is that individual patient data drive model predictions, through built-in variables, whose values are determined for each

Author contributions: V.C. developed diffusion-based drug resistance model; E.L.B. and V.C. designed research; E.L.B. obtained histopathological material and performed pathological diagnostics; E.J.K. obtained CT scans; S.A.C. identified subjects; J.P., E.L.B., Z.W., and V.C. performed research; J.P., E.L.B., Z.W., E.J.K., S.A.C., and V.C. analyzed data; and E.L.B. and V.C. wrote the paper.

The authors declare no conflict of interest.

*This Direct Submission article had a prearranged editor.

Freely available online through the PNAS open access option.

[1]J.P., E.L.B., and Z.W. contributed equally to this work.

[2]To whom correspondence should be addressed. E-mail: VCristini@salud.unm.edu.

This article contains supporting information online at www.pnas.org/lookup/suppl/doi:10.1073/pnas.1300619110/-/DCSupplemental.

www.pnas.org/cgi/doi/10.1073/pnas.1300619110

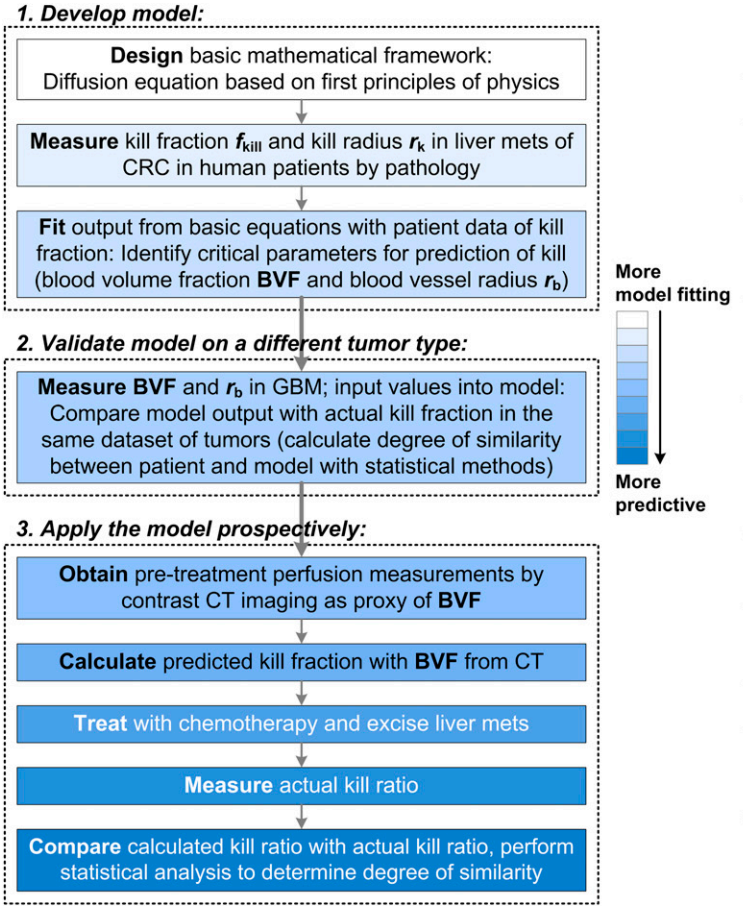

Variable	Definition
f_{kill}	Fraction of dead tumor measured in the patient tissue
$f_{kill}^{M}(\sigma_0)$	Fraction of dead tumor in monolayer assays *in vitro* (a property of the cell, the drug dose and type; herein assumed = 1)
r_b	Radius of drug source (fitted, Fig. 4; measured as equivalent portal triad radius in liver, or vessel radius in brain, Fig. 6)
BVF	Blood volume fraction (fitted, Fig. 4; measured as ratio of blood vessel-to-viable tumor area in histopathology, Fig.6, or from CT scans using Eq. 4, Fig. 7*B*)
L	Diffusion penetration distance (fitted, Fig. 4; calculated from Eq. 3, Fig. 6)
r_k	"Kill radius," measured thickness of dead tumor surrounding the drug sources
σ_0	Drug concentration in the blood source
σ_k	Threshold drug concentration for cell kill: $f_{kill}^{M}(\sigma \le \sigma_k) = 0$

Fig. 1. Process diagram of model development and application (*Left*). Definitions of variables (*Right*).

patient from standard clinical diagnostic tests. This introduces mechanistic, predictive modeling into personalized medicine.

Methods

The process to predict patient response to chemotherapy (Fig. 1) begins with model development, from equations based on the first principles of physics that describe diffusion within the tumor and organ tissue, and assumptions that define the spatial domain of tissue and tumor in which the equations apply (Fig. 2).

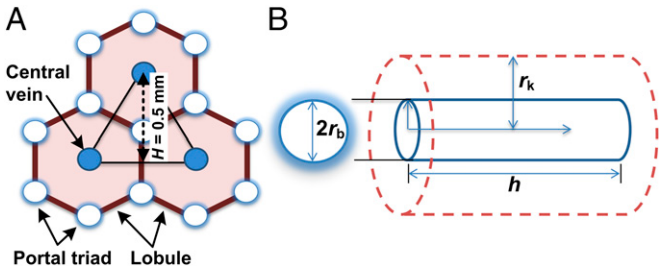

Fig. 2. Definition of tissue domain where the model equations are solved. (*A*) Hexagonal, cylindrical microscopic structure of liver. (*B*) Liver: idealized cylindrical portal triad; brain: an individual blood vessel segment between bifurcations. r_b and h: radius and length of drug source, of large aspect ratio ($2 \cdot r_b \ll h$); r_k: "kill radius," that is, thickness of dead tumor region. The diffusion penetration distance L is assumed to determine r_k and is calculated using Eq. 3; the blood volume fraction BVF is calculated from the measurements of cross-sectional areas of the sources (Fig. 1 and *Methods*).

Assumptions About Tissue Architecture and Drug Diffusion. Metastasizing cells from CRC are carried via the portal vein from the intestine to seed the liver, where they may implant and grow. Systemic chemotherapy also enters the liver parenchyma from the portal triad (Fig. 2*A*). Barriers to drug delivery within the tumors include their own induced vasculature and microenvironment. We model the movement of drug molecules through the sinusoidal system as a percolation described by an effective diffusion coefficient. For GBM, we assume a relatively isotropic distribution of blood vessels and effective drug diffusivity (Fig. 2*B*).

Here, the diffusion of drug molecules is modeled to follow extravasation from a single straight cylindrical source of large aspect ratio: $r_b \ll h$ (Figs. 1 and 2*B*). For the unique case of the liver, this idealized source encompasses the entire portal triad (Fig. 2*A*), whereas for the brain this source is a single blood vessel (Fig. 2*B*). Diffusion and cellular uptake within the surrounding cylindrical volume of tumor tissue (Fig. 2*B*, red dashed lines) are modeled assuming that the distances between the sources (i.e., portal triads in liver or vessels in brain) are significantly larger than the diffusion penetration distance L ($H \gg L$; H = 0.5 mm for the liver, Fig. 2*A*). Within a metastatic liver tumor the vasculature is different from that of adjacent healthy liver. In the liver both normal vessels and sinusoids, while in metastasis tumor vessels, are sources of drug.

Mathematical Modeling of Tumor Kill. The model variables and parameters are defined in Fig. 1; see *SI Text* for details and formulas. Local drug concentration within the tumor is calculated by solving an equation that describes the diffusion and uptake of drug by tumor cells after extravasation. The fraction of tumor cells killed depends on this local concentration within the tumor and on the effectiveness of the drug at that concentration (e.g., as measured in a monolayer assay in vitro). Therefore, the fraction of tumor kill f_{kill} is computed here by averaging this drug effectiveness over the cylindrical volume surrounding the source (Fig. 2*B*, dashed lines). This approach enables the model to account for both the pharmacokinetics–pharmacodynamics of drug cytotoxicity as well as drug penetration heterogeneity across the tumor tissue. The fraction f_{kill}, in the presence of a concentration σ_0 of

drug in the blood, and the corresponding kill radius r_k are obtained as the unique solutions of the following equations:

$$f_{kill} = f_{kill}^{M}(\sigma_0) \cdot BVF \cdot \frac{2Lr_b \cdot K_1(r_b/L) - 2Lr_k \cdot K_1(r_k/L) - (r_k^2 - r_b^2) \cdot K_0(r_k/L)}{r_b^2 \cdot (K_0(r_b/L) - K_0(r_k/L))}, \quad [1a]$$

$$\frac{\sigma_k}{\sigma_0} = \frac{K_0(r_k/L)}{K_0(r_b/L)}. \quad [1b]$$

K_0 and K_1 are modified Bessel functions of the second kind of orders 0 and 1, respectively (12). (Drug dosing and timing will affect the local value of drug concentration in tumor and surrounding tissue at any time during treatment. Because this information is currently unavailable from clinical tests, we replace this time-fluctuation with an equivalent, effective time-averaged value of drug concentration in the blood σ_0.)

Histopathology Measurements. H&E-stained microscopic slides of randomly selected human liver specimens removed from 10 patients and GBM specimens from a second cohort of 8 patients, all after chemotherapy, were obtained from Rhode Island Hospital pathology service, University of New Mexico Human Tissue Repository, and Cooperative Human Tissue Network (CHTN), a National Cancer Institute-supported human tissue repository at six different academic medical centers, according to Brown University and Rhode Island Hospital, University of New Mexico (UNM) and CHTN institutional review board human subject approvals. Eight liver specimens showed well-differentiated metastatic colorectal adenocarcinoma with minimal inflammatory component. Two were eliminated as failing to meet this criterion: one had mucinous, poorly differentiated cancer and the other intense inflammatory patterns. Four GBM specimens were large enough to be usable. Automated imaging of each entire specimen was performed with bright-field illumination with an Acroplan 4× objective on a fully mechanized Zeiss Axioscope ZO1 running Axiovision 4.8 with Mosaic software and captured on a Zeiss Axiocam HR digital camera. Images were transferred to Photoshop for analysis and figure preparation. Similar procedures were used on a third cohort of specimens from 21 patients at the MD Anderson Cancer Center (MDACC). Six were not included in the analysis because blood vessels were not visible in the H&E-stained sections or in one case because the specimen was not large enough and thus relevant parameters could not be measured.

The fraction of tumor killed was directly measured as the fraction of tumor area killed from the histopathology images, by assuming that the histologic sections are isotropic. Fig. 3*B*, bottom, shows an illustration of the measurements, manually performed using GNU Image Manipulation Program (GIMP) (13), of the thickness of area occupied by dead tumor (the kill radius in red lines), from a representative histopathology specimen (Fig. 3*A*). To calculate the fraction of dead tumor area, the dead areas of tumor were colored red while the live areas of tumor were colored blue (Fig. 3*C*). Portions that were not tumor were colored green. The fraction of dead tumor area was set as:

$$f_{kill} = \#\text{ of red pixels}/(\#\text{ of red pixels} + \#\text{ of blue pixels}). \quad [2]$$

Areas of tissue exhibiting fibrosis were included, because chemotherapy has been directly shown to induce fibrosis in liver (14, 15). Owing to the large size of each histopathologic image, measurements of r_k and f_{kill} were made for up to 12 evenly subdivided images (of size $>L$) to obtain a statistically meaningful ensemble for measurements of mean and SD, for each of the liver and brain samples, to generate the results in Figs. 4–7. The highest and lowest outliers that were >2 SDs from the mean were removed before the analysis in Fig. 4. The accuracy of the image segmentation procedure was verified by comparison of the distribution of f_{kill} values from the histopathology of the third cohort of patients (MDACC), measured using the GNU Image Manipulation Program by the UNM group, with those directly assessed by the pathologist (Fig. S1 and *SI Text*).

Regression and Statistical Analyses. Herein, *P* values obtained from data fitting using a model (i.e., linear regression, Eq. **1a**, or Eq. **3**) indicated that the null hypothesis that the model parameters are not significant should be rejected. The same *P* values were obtained using both Mathematica (16) and the software Prism in Graphpad (17). Least-squares fitting (18) of Eq. **1a** was performed using Mathematica routine "NonlinearModelFit" (16) to the kill fraction and kill radii measured in liver metastasis in the CHTN patient cohort. This resulted in estimates of parameters blood volume fraction (BVF), r_b, and L, which produced the best fit. An independent two-sided, two-sample Student *t* test resulted in $P = 0.46$, indicating differences between the data obtained from histopathology and output of the mathematical model were not significant (i.e., $P > 0.05$). Following this up with an equivalence test further demonstrated that the two groups were equivalent, with >95% confidence, and that the sample size was sufficient (*SI Text*).

Test of Model Predictivity. Eqs. **1a** and **1b** can be combined to eliminate σ_k and r_k, and thus obtain the (maximum) predicted f_{kill} for each patient as a function solely of parameters r_b, BVF, and diffusion penetration distance L, all of which can be directly measured from histopathology or imaging:

$$f_{kill} = 2 \cdot BVF \cdot L \cdot \frac{\sqrt{BVF} \cdot K_1(r_b/L) - K_1\left(r_b/\left(L \cdot \sqrt{BVF}\right)\right)}{\sqrt{BVF} \cdot r_b \cdot K_0(r_b/L) \cdot (1 - BVF)}, \quad [3]$$

where integration was practically executed up to a distance that scales with the intersource distance $\propto r_b/\sqrt{BVF}$ (*SI Text*). [The fraction of cells killed in the absence of diffusion gradients was assumed to be $f_{kill}^{M}(\sigma_0) = 1$. We assumed that the amount of drug in the vasculature would be sufficient to kill all cells in vitro. Therefore, this parameter is omitted herein.] Here Eq. **3** was tested on the MDACC cohort of patients with CRC metastatic to liver by using the same input parameter values for r_b and L obtained from the regression analysis of the CHTN cohort. A graph was generated by comparing the predictions of Eq. **3** to the direct measurements of kill (Fig. 7*A*).

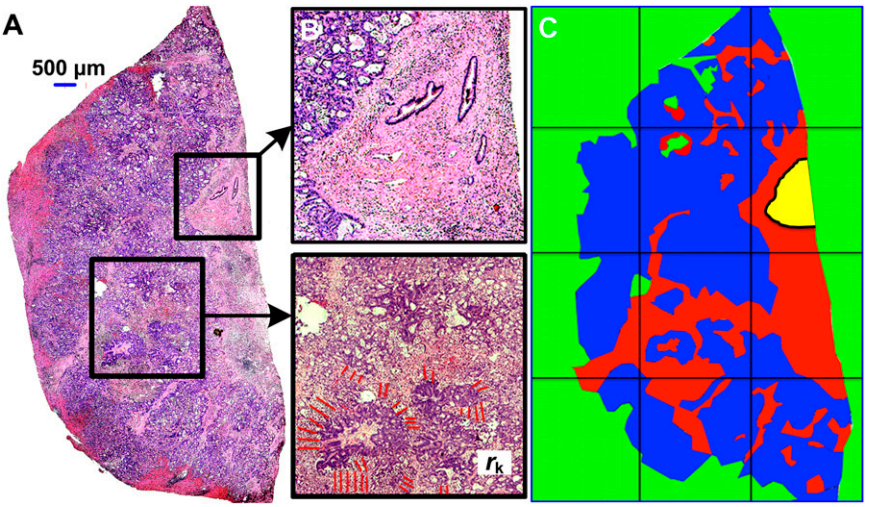

Fig. 3. Example of measurements from histopathological specimens. (*A*) Histologic section from the first cohort showing the entire slide. (*B*) Example of portal triad and central vein (*Upper*) and of measurements of the kill radii r_k (red lines) around tumor nodules (*Lower*). (*C*) Segmentation of *A* for calculation of the fraction of dead tumor area (Eq. **2**): dead tumor (red); live tumor (blue); no tumor (green); portal triad and central vein (yellow).

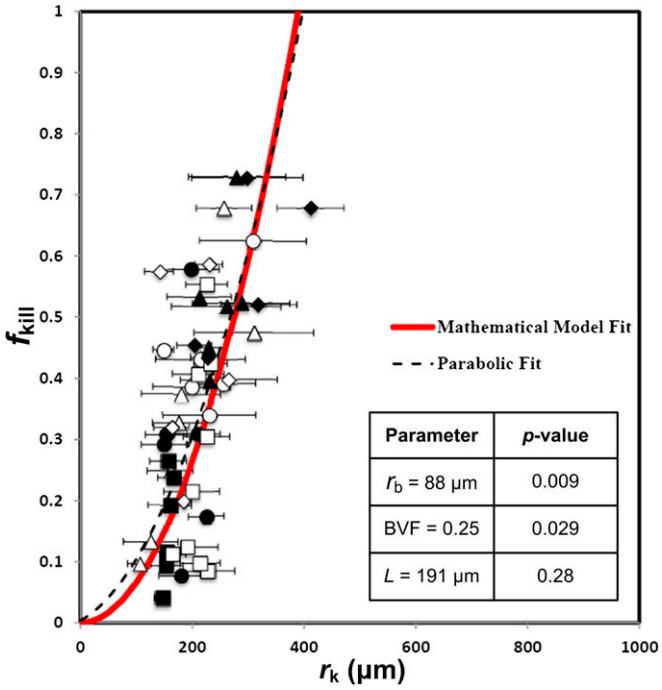

Fig. 4. Fitting the model to patient data demonstrates biological accuracy of the functional form of Eq. **1a**. Symbols: measurements from 49 histology images of CRC metastatic to liver in the first cohort of patients (*Methods*), with SDs (six measurements per tumor nodule). Dashed line, quadratic least-square fit; red line, least-square fit of Eq. **1a** to the data (coefficient of determination $R^2 = 0.92$; $R^2 = 0.94$ between the two curves). (*Inset*) Parameter values obtained from fit.

Model Validation in a Different Tumor Type. Model parameters r_b and BVF were directly measured from each GBM patient brain specimen together with the fraction of tumor killed, to solve Eq. **3** directly for the diffusion penetration distance L, thus fully constraining the model without fitting. A graph was then generated by entering these parameter values into Eq. **1a** and comparing the resultant output produced by the calculations to the direct measurements of kill in each patient (Fig. 6; also see Fig. S2).

Prospective Application of the Model Based on Pretreatment CT Scans. Contrast CT scans performed according to standard clinical protocols (19) were acquired before chemotherapy on 11 patients at MDACC according to institutional review board-approved protocols. The simple average of three Hounsfield unit (HU) measurements in representative areas within the entire tumor was calculated at each phase of the test for each patient (Fig. 7*B*, *Inset*), that is, a late arterial phase (30–35 s after start of contrast injection), a portal venous phase (50–55 s), and a delay phase (minutes, variable timing).

The pretreatment CT measurements (HU) at the arterial phase were found by linear regression analysis to correlate to the measurements of BVF (blood volume fraction) performed from posttreatment histology (*SI Text* and Fig. S3):

$$\mathrm{BVF} = 0.00088 \cdot \mathrm{CT}\ (\mathrm{HU}), \qquad [4]$$

with coefficient of determination $R^2 = 0.67$ (20), $P = 0.004$, from Mathematica routine "LinearModelFit" (16) and GraphPad Prism (17). CT measurement error of 25% was estimated from corresponding data of contrast enhancement in the aorta, and thus represents variability in physiology and contrast dosing in CT protocol across patients. Even with a limited number of subjects, the statistical significance ($P = 0.004$) is expected because CT measurements reflect perfusion of tissue, which relies on the volume fraction of blood vessels. Analysis using the portal–venous measurements produced similar results. Eq. **4** (with SD from the assessed CT measurement error) was used as input into Eq. **3** to generate a graph with model predictions of cell kill (with SD) for each patient and compared with the direct measurements from histopathology (Fig. 7*B*). The average relative error between the model prediction $f_{kill}(P)$ and the measured kill value $f_{kill}(M)$ was calculated as $\langle |(f_{kill}(P) - f_{kill}(M))/f_{kill}(M)| \rangle$.

Results

We pursued a three-step process to develop our mathematical model, obtain parameter values, apply the model to different tumor types, and then investigate the clinical relevance in prospective studies (Fig. 1). The first step involved building a mathematical equation based on diffusion incorporating a number of variables whose values were determined from histopathology and imaging data from individual patients. The boundary conditions of liver anatomy needed to solve the diffusion equation are illustrated in Fig. 2. For the case of the liver, the parameters r_b (equivalent radii of liver portals) and L (drug diffusion penetration distance) could be quantified from a regression analysis of all patient data (step 1). The parameter BVF was found to be the most sensitive and critical. Once these parameter values are determined for each individual patient, the mathematical model produces patient-specific predictions of the fraction of cells killed by chemotherapy. Model validation in a different tumor type, GBM, followed (step 2), and then led to its prospective application based on pretreatment measurements of BVF by contrast-enhanced CT scans (step 3 as diagrammed in Fig. 1).

Fitting the Mathematical Model to Patient Data by a Regression Analysis Identifies Biologically Realistic Parameter Values. Fraction of tumor killed f_{kill} and thickness of dead tumor regions r_k were measured in histopathological sections of metastatic CRC in liver after chemotherapy from the first cohort of patients (Fig. 3). Output from Eq. **1a** was directly fit by regression analysis to these tumor measurements (Fig. 4). This analysis demonstrated agreement of the functional form of Eq. **1a** with the distribution of patient data (Fig. 4; note the red curve approximation with symbols for patient data). We also applied a three-step statistical analysis to test the difference or equivalence of the distribution of our model predictions with our data, and that sample size of our data were large enough to have confidence in the results. This analysis found no statistically significant difference between the model predictions and the data [$P = 0.46$ in student t test (17)], but rather established that the data were equivalent (95% confidence interval) and that the sample size was adequate (*SI Text*).

The regression analysis resulted in estimates of the three parameters: r_b, L, and BVF (Fig. 4, *Inset*). Each of these estimated values is consistent with measurements from human anatomy. The radius of portal vessels, $r_b \approx 88$ μm, is consistent with the combined radii of hepatic artery and portal vein within portal triads in normal liver (21) and with those in our histopathology of these specimens (Fig. 3*A* and *B*). The value of BVF =

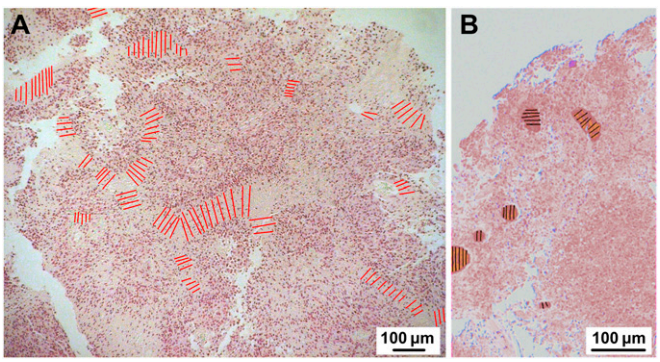

Fig. 5. Measurements from GBM histopathology. (*A*) Example with measurements (red) of kill radius r_k in an H&E-stained section of GBM biopsied after chemotherapy. (*B*) Example of a different GBM showing measurements of vessel diameters (lines across vessels) for calculation of the cross-sectional area and vessel-to-tissue fraction BVF. Such areas provide an underestimate of BVF because the smaller vessels not containing red blood cells are not visualized or counted.

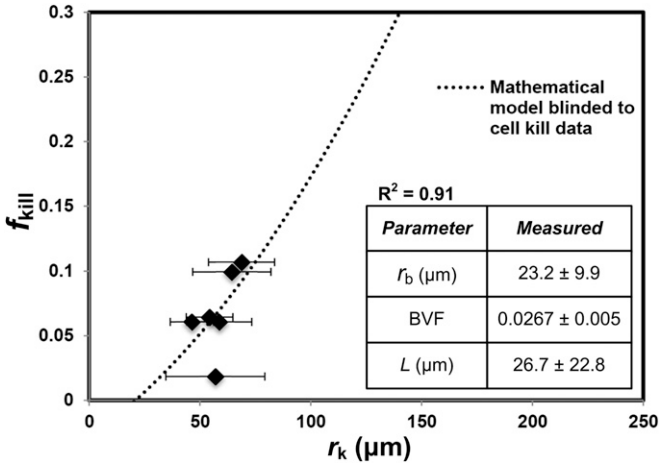

Fig. 6. Validating the model in GBM. Patient-specific predictions of Eq. **1a** (dotted line) vs. direct measurement of fraction of tumor kill f_{kill} (and kill radius r_k) from histopathology of biopsies after chemotherapy for one patient (symbols with SDs; seven images, 79 measurements total). (*Inset*) Input parameters BVF and r_b measured from histopathology. Parameter L was calculated using Eq. **3** from the measurements of the other parameters (*Methods*). See *SI Text* for similar results from three additional patients (Fig. S5).

0.25 obtained from the fit of the first cohort of patients (Fig. 4, *Inset*) is consistent with the range of values measured from all patient liver specimens in our third cohort, that is, BVF ≈ 0.01 −0.5 (Fig. 7*A*). [The blood volume fraction estimated by calculating the ratio between the portal vessels, i.e., structure containing blood, and lobule volumes assuming a hexagon of side length $H = 0.5$ mm (Fig. 2*A*), $\mathrm{BVF} \propto 4\pi/(3\cdot\sqrt{3})\cdot(r_b/H)^2$, is validated from histopathology measurements (*SI Text* and Fig. S4).] The diffusion penetration length from regression analysis is $L = 191$ μm. The latter result is corroborated by a simple scaling argument estimating $L \sim r_b/\sqrt{\mathrm{BVF}}$, proportional to the interportal distance, which, using the values of r_b and BVF from the fit, would give $L =$ 186 μm. The model's R^2 was 0.92 with the raw data and 0.94 with the simple parabolic fit $5.03\cdot10^{-6}\cdot r_k^2 + 6\cdot10^{-4}\cdot r_k + 3.6\cdot10^{-3}$ (Fig. 4). Using Mathematica (16), statistically significant P values were obtained for all parameters (Fig. 4, *Inset*), except for L ($P =$ 0.28). This suggests that the parameter L should be less variable from patient to patient, at least for the case of CRC metastatic to liver. We demonstrated above that the value of L obtained from this fit is consistent with that calculated from the histopathology measurements of r_b and BVF.

Additional testing of our model was performed by revisiting in vitro experiments on MCF-7 breast cancer cell lines (9), in which the measured ratio f_{kill}/f_{kill}^{M} of cells killed in 3D tumor spheroids in the presence of diffusion gradients of doxorubicin to cells killed in monolayers with no diffusion gradients was 0.3, comparable to the average fraction of kill $f_{kill} = 0.36$ calculated by averaging all measurements reported in Fig. 4.

Validation of the Model in a Different Tumor Type. We compared predictions of patient-specific cell kill from Eq. **1a** to the direct measurements from histopathology of GBM from a cohort of patients biopsied after chemotherapy (Fig. 5). In these specimens distinct large blood vessels were apparent that also allowed for measurements of blood vessel radii, r_b (Fig. 5*B*), and BVF. Thus, Eq. **1a** was fully informed from direct measurements (Fig. 6). Despite the heterogeneity of parameter values across different individuals (Fig. 5, *Inset* and Fig. S5, *Insets*), the model provided case-specific predictions of fraction of tumor killed, f_{kill}, in each patient with a high degree of accuracy ($R^2 = 0.91$; Fig. S5 shows three additional cases, where $R^2 = 0.89$, 0.86, and 0.74). The diffusion penetration distance L for brain tumors, calculated by solving Eq. **3** (*Methods*), was found to be smaller than for tumors in liver, which may be because the sinusoidal system in liver leads to better transport of the drug throughout the normal liver parenchyma surrounding the tumor nodules. Consistently, the fraction of tumor killed is lower for GBM, despite its vascular proliferation, possibly owing to less effective kill or lower rate of extravasation from thick-walled vessels found in GBM. These results demonstrate the general applicability of our approach, as well as the model's predictive power and translational value in different cancers.

Prospective Application of the Mathematical Model in Vivo. Next, we proceeded to apply the model in a clinical setting. We obtained a larger cohort of patients with CRC metastatic to liver (MDACC),

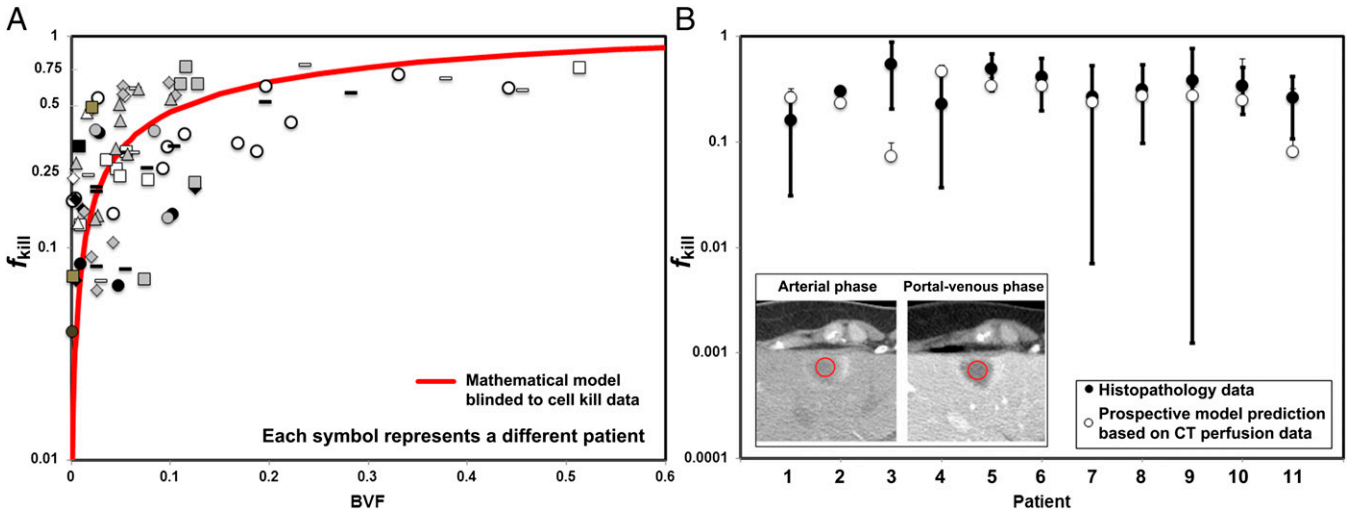

Fig. 7. Prospective, patient-specific model predictions match outcomes of fraction f_{kill} of cells killed by chemotherapy in a third cohort of patients with CRC metastatic to liver. (*A*) Testing of Eq. **3** from posttreatment histopathology (red, coefficient of determination $R^2 = 0.79$). (*B*) Predictions of Eq. **3** using the BVF parameter calculated (Eq. **4**) from pretreatment contrast-enhanced CT scan measurements (open circles, average relative error ~15% between prediction and actual). Multiple measurements per patient are indicated by the same symbol (*A*) and SD (*B*, filled circles). Model input parameters r_b (radii of liver portals) and L (drug diffusion penetration distance) from Fig. 4. (*B*, *Inset*) Examples of (*Left*) late arterial phase and (*Right*) portal–venous phase from contrast CT scans of a 2.4-cm hypodense CRC metastasis in the left anterior hepatic lobe (red circles indicate example of area used for measurement).

where pretreatment contrast CT scans were performed, followed by chemotherapy and surgical excision. To establish whether our model could predict chemotherapy outcome based only on standard pretreatment contrast CT imaging, we carried out the following series of steps. First we performed an analysis on the histopathology from posttreatment specimens similar to that described for the GBM. This again validated the predictive power of Eq. **3** specifically for this third cohort of patients (Fig. 7*A*, red curve: $R^2 = 0.79$). Because here we used the same value of diffusion penetration distance L and portal radius r_b obtained from the fit of the first cohort (Fig. 4), these results again point to uniformity of these parameters across patients, thus generating the hypothesis that future clinical translation would primarily rely on patient-specific calculation of the parameter BVF. To test this hypothesis we calculated a linear correlation constant for histopathology BVF and contrast CT Hounsfield units, which allowed us to obtain a BVF value from the contrast enhancement of the CT images for each individual (Eq. **4**). Inputting this value into Eq. **3** produced accurate kill-ratio predictions (Fig. 7*B*, open circles) that compared well to the actual measurements from histopathology posttreatment (Fig. 7*B*, filled circles), with an average relative error of the predicted fraction killed of ~15% (*Methods*).

Discussion

We provide a mechanistic approach towards understanding the relationship between drug perfusion and tumor death. Through an analysis of patient histopathology specimens of CRC metastatic to liver and of GBM, we show that our model successfully predicts virtually the entire range of patient responses ($4\% < f_{kill} < 90\%$). We illustrate the model's potential for prospective application in the clinic by predicting cell kill in additional patients with CRC metastatic to liver based on input data obtained from contrast-enhanced CT scans before treatment. Our predictive, prospective model is generally applicable across tumor types and is valid for both CT imaging and histopathology, is applicable to immunotherapy (22) as well as other types of chemotherapy, and also likely to be useful beyond the context of cancer in any case where drug delivery relies on local perfusion properties.

We demonstrate that physical processes significantly influence complete eradication of solid tumors via conventional chemotherapy as currently administered, because tumor kill induced by passively transported drug molecules is limited by the survival of tumor cells within the diffusion length L. Together, the results from this study provide insights into how cancer treatment fails. Characteristics such as blood source radius and blood volume fraction that are measurable in histopathological specimens, or from imaging before chemotherapy, can be directly used in the mathematical model to predict responses and to develop and monitor patient-specific treatment strategies. Approaching clinical oncology as an engineering problem will promote the design of successive chemotherapy cycles based on the diffusivity within individual tumors as determined by Eqs. **1** and **3**. Such basic knowledge of tumor's physical properties will drive dosage and timing and may contribute to discovery of novel delivery mechanisms (e.g., using drug nanocarriers that are rationally designed to maximize cell kill while minimizing toxicity effects).

The strength of the model presented here is in the ability to quantify chemotherapeutic response in CRC metastatic to liver and in GBM based on parameter values that are readily measurable in standard clinical tests. Application to some types of solid tumors where vasculature is very heterogeneous or dense, and fibrous tissue is present will require additional mathematical formulations for diffusivity D and uptake rate of drug λ (*SI Text*) as functions of the tumor microenvironment, such as its characteristics as a heterogeneous viscous fluid model or its porosity (23). Remarkably, only three parameters were necessary to predict tumor kill fractions matching actual outcomes with 15% average error. The focus of this study was on the drug effect alone, based on histopathological samples of well-differentiated disease, which provided clear distinction between liver and dead tumor regions. The model presented here provides a mathematical framework upon which additional layers of formulation may incorporate cellular heterogeneity in more poorly differentiated tumors, hypoxia, fibrosis, and inflammation.

ACKNOWLEDGMENTS. We thank A. Day, T. Brocato, R. Kerketta, J. Butner, P. Dogra, and Z. Harris (V.C. laboratory); K. Kilpatrick, A. Gonzales, and R. O'Connor (E.L.B. laboratory); and M. Loewenberg, R. Broaddus, D. Kirui, M. Ferrari, and H. Frieboes. This work was supported by National Institute of General Medical Sciences (NIGMS) Grant K12GM088021 (to J.P.); National Cancer Institute Grant CA153825, NIGMS Grant P50GM085273, National Institute of Neurological Disorders and Stroke Grant NS062184, and a Harvey Family Professorship (to E.L.B.); Center for Transport Oncophysics Physical Sciences-Oncology Center (CTO PS-OC) Grant 1U54CA143837 (to S.A.C. and V.C.); Texas Center for Cancer Nanomedicine Grant 1U54CA151668, USC PS-OC Grant 1U54CA143907, Integrative Cancer Biology Program Grant 1U54CA149196, and University of New Mexico Cancer Center Victor and Ruby Hansen Surface Professorship in Molecular Modeling of Cancer (to V.C.).

1. Edgerton ME, et al. (2011) A novel, patient-specific mathematical pathology approach for assessment of surgical volume: Application to ductal carcinoma in situ of the breast. *Anal Cell Pathol (Amst)* 34(5):247–263.
2. Cui Y, Zhang X-P, Sun Y-S, Tang L, Shen L (2008) Apparent diffusion coefficient: Potential imaging biomarker for prediction and early detection of response to chemotherapy in hepatic metastases. *Radiology* 248(3):894–900.
3. Rubin E, Reisner HM (2009) *Essentials of Rubin's Pathology* (Lippincott Williams & Wilkins, Philadelphia).
4. Quan D, et al.; Surgical Oncology Program at Cancer Care Ontario (2012) The role of liver resection for colorectal cancer metastases in an era of multimodality treatment: A systematic review. *Surgery* 151(6):860–870.
5. Leonard GD, Brenner B, Kemeny NE (2005) Neoadjuvant chemotherapy before liver resection for patients with unresectable liver metastases from colorectal carcinoma. *J Clin Oncol* 23(9):2038–2048.
6. Cho K, Wang X, Nie S, Chen ZG, Shin DM (2008) Therapeutic nanoparticles for drug delivery in cancer. *Clin Cancer Res* 14(5):1310–1316.
7. Jain RK (2005) Normalization of tumor vasculature: An emerging concept in antiangiogenic therapy. *Science* 307(5706):58–62.
8. Sinek J, Frieboes H, Zheng X, Cristini V (2004) Two-dimensional chemotherapy simulations demonstrate fundamental transport and tumor response limitations involving nanoparticles. *Biomed Microdevices* 6(4):297–309.
9. Frieboes HB, et al. (2009) Prediction of drug response in breast cancer using integrative experimental/computational modeling. *Cancer Res* 69(10):4484–4492.
10. Minchinton AI, Tannock IF (2006) Drug penetration in solid tumours. *Nat Rev Cancer* 6(8):583–592.
11. Soda Y, Myskiw C, Rommel A, Verma IM (2013) Mechanisms of neovascularization and resistance to anti-angiogenic therapies in glioblastoma multiforme. *J Mol Med (Berl)* 91(4):439–448.
12. Kreyszig E (2010) *Advanced Engineering Mathematics* (Wiley, New York).
13. The GIMP Team (2013) GNU Image Manipulation Program. Available at http://docs.gimp.org/odftest/en.pdf.
14. Kandutsch S, et al. (2008) Patterns of hepatotoxicity after chemotherapy for colorectal cancer liver metastases. *Eur J Surg Oncol* 34(11):1231–1236.
15. Vauthey J-N, et al. (2006) Chemotherapy regimen predicts steatohepatitis and an increase in 90-day mortality after surgery for hepatic colorectal metastases. *J Clin Oncol* 24(13):2065–2072.
16. Wolfram Research (2008) Mathematica, Version 8.0, Mathematics and Algorithms. Available at www.wolfram.com/learningcenter/tutorialcollection/MathematicsAndAlgorithms/MathematicsAndAlgorithms.pdf.
17. GraphPad Software (2007) GraphPad Prism, Version 5.0, Statistics Guide. Available at www.graphpad.com/downloads/docs/Prism5Stats.pdf.
18. Smyth GK (2006) *Nonlinear Regression. Encyclopedia of Environmetrics* (Wiley, New York).
19. Ichikawa T, Erturk SM, Araki T (2006) Multiphasic contrast-enhanced multidetector-row CT of liver: Contrast-enhancement theory and practical scan protocol with a combination of fixed injection duration and patients' body-weight-tailored dose of contrast material. *Eur J Radiol* 58(2):165–176.
20. Devore JL (2011) *Probability and Statistics for Engineering and the Sciences* (Cengage Learning, Stamford, CT).
21. Crawford AR, Lin X-Z, Crawford JM (1998) The normal adult human liver biopsy: A quantitative reference standard. *Hepatology* 28(2):323–331.
22. Das H, et al. (2013) Impact of diffusion barriers to small cytotoxic molecules on the efficacy of immunotherapy in breast cancer. *PLoS ONE* 8(4):e61398.
23. Vafai K (2010) *Porous Media: Applications in Biological Systems and Biotechnology* (Taylor & Francis, New York).